

Time Resolved PIV Analysis of Flow Over a NACA 0015 Airfoil with Gurney Flap

D. R. Troolin, E.K. Longmire, W. T. Lai

Application Note PIV-014

D. R. Troolin, W. T. Lai, TSI Incorporated, 500 Cardigan Road, Shoreview, MN 55126, USA
E. K. Longmire, Department of Aerospace Engineering and Mechanics, University of Minnesota, Minneapolis, MN 55455, USA

Correspondence to:

D. R. Troolin, TSI Incorporated, 500 Cardigan Rd., Shoreview, MN 55126, E-mail: dan.troolin@tsi.com, Tel: 651-490-3885, Fax: 651-490-3824

Abstract A NACA 0015 airfoil with and without a Gurney flap was studied in a wind tunnel with $Re_c = 2.0 \times 10^5$ in order to examine the evolving flow structure of the wake through time-resolved PIV and to correlate this structure with time-averaged measurements of the lift coefficient. The Gurney flap, a tab of small length (1% to 4% of the airfoil chord) that protrudes perpendicular to the chord at the trailing edge, yields a significant and relatively constant lift increment through the linear range of the C_L vs. α curve. Two distinct vortex shedding modes were found to exist and interact in the wake downstream of flapped airfoils. The dominant mode resembles a Kármán vortex street shedding behind an asymmetric bluff body. The second mode, which was caused by the intermittent shedding of fluid recirculating in the cavity upstream of the flap, becomes more coherent with increasing angle of attack. For a 4% Gurney flap at $\alpha = 8^\circ$, the first and second modes corresponded with Strouhal numbers based on flap height of 0.18 and 0.13. Comparison of flow around “filled” and “open” flap configurations suggested that the second shedding mode was responsible for a significant portion of the overall lift increment.

1 Introduction

Aerodynamic design has seen a rise in the implementation of multifunctional devices and actuators that allow for dramatic changes in performance with only slight variations to the effective surfaces. Although rote airfoil design has essentially yielded its peak in performance, auxiliary mechanisms are being investigated and explored for their potential in making airfoils more functional, especially in demanding environments such as edge-of-the-envelope performance, unmanned, light and fast, and high-lift low-speed applications. The Gurney flap, a small tab approximately 1% to 4% of the airfoil chord in length that protrudes typically 90° to the chord at the trailing edge, is one such device. Recently, the flap has



been of interest in applications from banner-towing aircraft (see Wynbrandt 2002), to unmanned air vehicles (UAVs) as investigated by Solovitz and Eaton (2004a and b).

Originally used on a racecar in the 1970s by Daniel Gurney, for whom it is named, the flap was first studied at some length by Liebeck (1978), who first proposed the existence of counter-rotating vortices downstream of the flap. A subsequent study by Neuhart and Pendergraft (1988) at a Reynolds number of 8588 gave valuable qualitative information on the wake structure through visual observation of dye streaks. The Gurney flap was found to delay the separation on the suction surface of the airfoil for angles of attack less than 3.5° . In addition, a configuration in which the upstream cavity of the flap was filled was tested and found to diminish the “separation delay” benefit of the flap. Wadcock (1987) performed wind tunnel tests at a Reynolds Number of 1.64×10^6 on a baseline NACA 4412 airfoil. These tests showed a significant increase in the lift coefficient, shifting the lift curve up by 0.3 for a Gurney flap of 1.25% of the chord length, and providing a greater maximum lift. There was no appreciable increase in drag until the Gurney flap was extended beyond about 2% of the airfoil chord length, at which point the flap extended beyond the boundary layer thickness.

Storms and Jang (1994) used pressure sensors located around the surface of a NACA 4412 airfoil with Gurney flap to measure lift, drag, and pitching moment. The time-averaged results matched well with their RANS computations of the same airfoil. They found the Gurney flap to increase lift at all angles of attack. Jang et al. (1998) presented additional results of RANS computations based on the same airfoil shape suggesting that increases in lift coefficient resulted from increases in pressure difference along the entire chord of the airfoil with stronger increases near the flap.

Jeffrey et al. (2000) performed a comprehensive study on flapped airfoils including surface pressure and LDA measurements and flow visualization. The time-averaged velocity fields revealed a pair of counter-rotating vortices downstream of the flap consistent with earlier hypotheses by Liebeck and the RANS results of Jang et al. Spectra from the LDA measurements and smoke visualizations documented the presence of a Karman vortex street. The authors attributed the increase in lift caused by the flap to two causes: periodic vortex shedding downstream of the flap served to increase the trailing-edge suction of the airfoil, and the deceleration of the flow directly upstream of the flap contributed to a pressure difference acting across the trailing-edge. Time- and phase-averaged PIV analysis by Solovitz and Eaton (2004a and b) was used to gather additional information on the flow pattern around static and dynamically-actuated Gurney flaps.

This study quantifies the effects of a Gurney flap on a NACA 0015 airfoil through time-averaged force measurements, hot film anemometry, and time-resolved particle image velocimetry (TRPIV). Although it is well known that the flaps yield increased lift forces, the mechanisms behind the increases are still not well understood. TRPIV allows investigation of details of flow patterns that are not easily observed or quantified by other measurement techniques. In particular, TRPIV can be used to examine evolving flow fields in order to observe variations not associated with a “standard” vortex street. As will be described below, an additional shedding mode associated with the recirculation zone upstream of the flap appears to contribute significantly to the overall airfoil lift.

2 Experimental Apparatus and Methods

The experiments were conducted in the University of Minnesota Department of Aerospace Engineering Open Return Wind Tunnel which is blower driven. The test section was $0.6 \text{ m} \times 0.6 \text{ m}$. Hot-film anemometry measurements revealed a freestream turbulence intensity of less than 0.25%. Each airfoil section had a span (b) of 304.8 mm and a chord length (c) of 190.5 mm, resulting in an aspect ratio $A = 1.6$. The airfoils and flap attachments were fabricated in a rapid-prototype machine at the University of Minnesota Department of Aerospace Engineering and Mechanics. In the wind tunnel, the airfoil was mounted to a flat, circular plate and then to a sting, as shown in Figure 1, which entered the tunnel from the side so that it was horizontal and perpendicular to the freestream flow direction. In addition, the sting

was capable of rotating, so that various angles of attack could be set with an accuracy of approximately 0.2° .

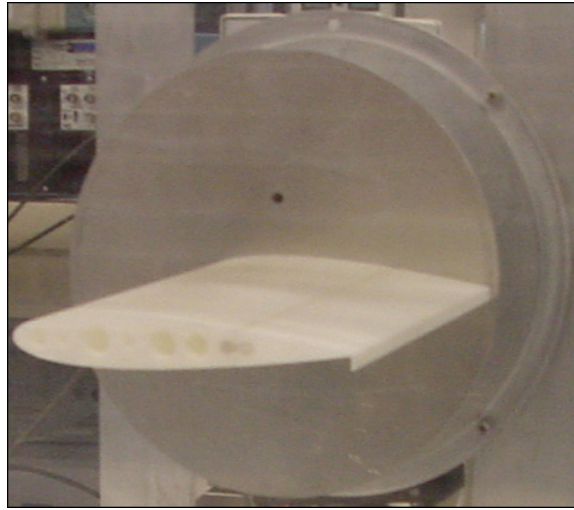


Figure 1: Airfoil section mounted in wind tunnel.

Four Gurney flap configurations were tested, with the length of the Gurney flap (h) measured relative to the total chord length of the airfoil from the tip of the flap to the chordline of the airfoil at the trailing edge: 0%, 1%, 2%, and 4%. This study concentrates on the airfoil with the largest flap which is approximately twice the thickness of the boundary layer as determined using Blake's (1986) estimate of displacement thickness for blunt trailing edges. In addition to the flapped airfoils, a "closed" flap configuration (4%) was also tested (Figure 2), in which the upstream cavity of the Gurney flap from the tip to the point $0.30c$ from the trailing edge on the pressure side of the airfoil, was filled in. This arrangement made it possible to determine the direct influence of the upstream recirculation region on the downstream wake.



Figure 2: "Closed" flap configuration.

The control configuration consisted of a NACA 0015 symmetric airfoil with no flap. This shape was chosen as a very common airfoil (with a large body of experimental data available) with a fairly simple design. The force measurements, hot-film anemometry, and TRPIV data were conducted at a freestream velocity of $U_\infty = 15.4$ m/s. The Reynolds number based on chord length was 2.0×10^5 . The freestream velocity was chosen to provide the largest possible Reynolds number while maintaining stability within the airfoil mounting apparatus.

The wind tunnel sting provided three-component force and moment measurements. The sting was tared at each angle of attack before data acquisition. Fifty readings were taken over the course of 90 seconds and averaged to determine the lift coefficient for each configuration. When the data were corrected for finite aspect ratio and compared with values published by NACA (National Advisory Committee on Aeronautics) on the same airfoil section, the C_L values and lift curve slope of the control airfoil matched within 0.2% of the same airfoil section tested at a Reynolds number of 2.2×10^5 (see Jacobs and Anderson 1930 and Jacobs and Sherman 1937).

Hot-film anemometry measurements were taken with a $50 \mu\text{m}$ diameter platinum-coated quartz substrate sensor with a sensing length of 1 mm. The original measurement location was $0.5c$ directly downstream of the trailing edge for the airfoil without a Gurney flap, and $0.5c$ directly downstream of the flap tip for the 4% Gurney airfoil. Further measurements were acquired at additional locations described in the results section. Power spectra were obtained from samples of 8,000 points collected at a sampling rate of

2,000 Hz for the wake Strouhal number ($St = fh/U_\infty$) vs. angle of attack calculations, and 64,000 pts collected at a sampling rate of 4,000 Hz for the calculation of Strouhal number at various locations around the flap. Spectra were also determined independently using TRPIV velocity field data, to assess the validity of this method for calculating spectra. In this case, the FFT was performed on the fluctuating velocity component normal to the freestream direction (v') averaged over a column of vectors spanning the wake at $0.5c$ downstream of the trailing edge. The sampling rate was 1,000 Hz; the number of samples was 1000.

TRPIV is a simple extension of the standard PIV technique described well by Adrian (1991) whereby images are acquired at a faster rate. For this experiment, images were acquired at approximately the center of the wind tunnel span and center of the airfoil section, with the goal of minimizing 3-D effects occurring near the wingtip. In addition, measurements were made in two configurations. The first was with the laser light sheet entering from the exit of the tunnel, and the second with the light sheet entering the tunnel from above, with the camera mounted on the side of the tunnel in both cases, as seen in Figure 3. The data from the second configuration was inverted in the subsequent plots for purposes of comparison. These two configurations allowed velocity information to be gleaned from the area directly downstream of the Gurney flap, as well as from the cavity directly upstream of the flap.

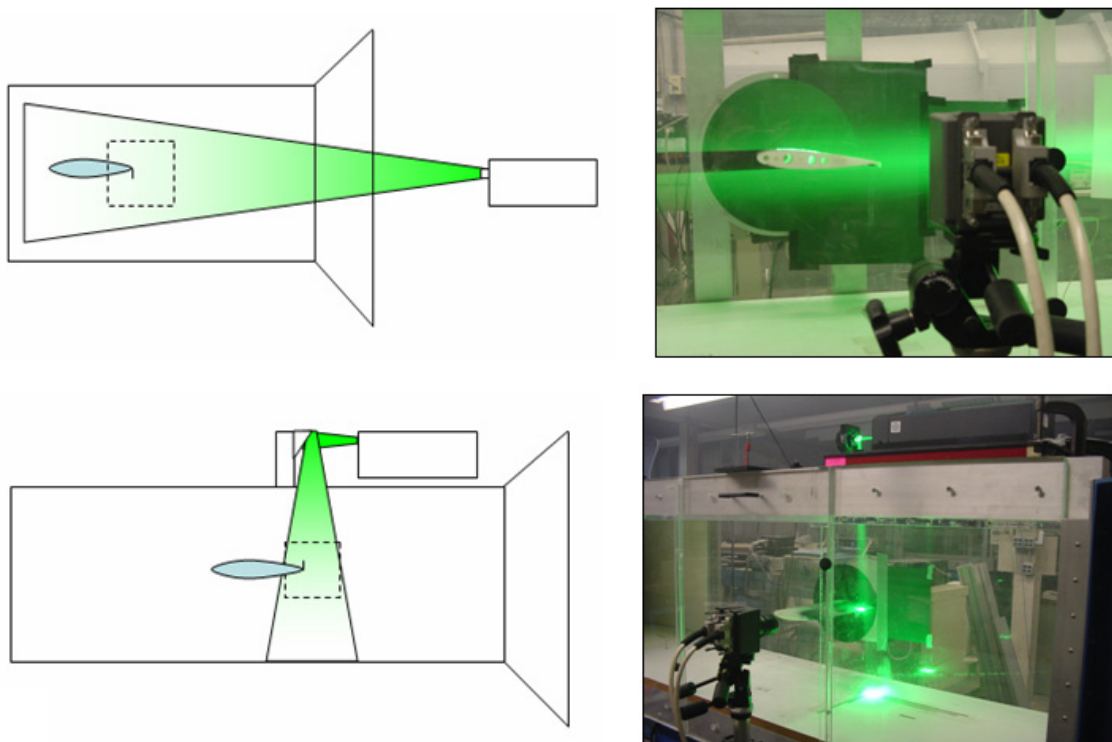


Figure 3: Schematic of the experimental setup in the wind tunnel.
Upper two Figures show configuration one; lower two Figures show configuration two.

Two 25 W diode-pumped Nd:YLF lasers emitted light of wavelength 527 nm with pulse width of 135 ns, beam diameter of 1.5 mm, and divergence of 3 mrad. The two beams were combined to travel on co-linear paths. Coplanar light sheets were generated with a cylindrical lens to diverge the incident laser beams in one direction; the divergence was controlled by the focal length of the lens which was -25 mm. A spherical lens controlled the thickness of the sheet by focusing it in the direction normal to the plane of the sheet. At the measurement region, the thickness was approximately 1 mm. Each laser could be operated over a range of pulsing frequencies with the energy per pulse decreasing as the pulse frequency increased. At 1000 Hz, the energy per pulse was 10 mJ, and at 4000 Hz the energy per pulse was 4 mJ.

Digital image sequences were acquired from a 10-bit CMOS high speed camera at rates of 2000 frames per second, 4000 frames per second, and 8000 frames per second, which correspond to velocity field capture rates of 1000 Hz, 2000 Hz, and 4000 Hz, respectively. The pixel size was 9 microns. In this paper, we concentrate primarily on the data captured at 2000 frames per second with camera resolution of 1024 by 1024 pixels, and on data captured at 4000 frames per second with pixel resolution of 1024 by 512 pixels (Some of the data were captured at 8000 frames per second with pixel resolution of 1024 by 256, but only every second field is shown for purposes of clarity). Higher frequencies were attempted, but the laser illumination energy was too low to produce meaningful results. A 50 mm lens was used with a largest aperture setting of f#1.4. The full field of view ranged from $(123 \text{ mm})^2$ to $(141 \text{ mm})^2$ depending on the distance to the measurement region which changed slightly for the various flap configurations. Olive oil atomized with an array of six Laskin nozzles was used to seed the flow providing droplets with a mean diameter between 1 μm and 3 μm .

The camera frames and laser pulses were synchronized with a TSI synchronizer with 1 ns resolution. The pulses from each laser were timed to straddle neighboring camera frames in order to produce images suitable for PIV cross-correlation (Figure 4). The time between frame-straddled laser pulses (Δt) was 35 μs , which allowed for a maximum particle displacement of 4 pixels at $U_\infty = 15.4 \text{ m/s}$.

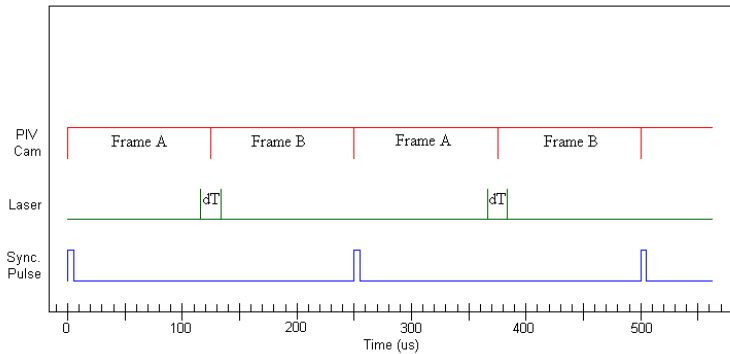


Figure 4: Typical timing diagram for PIV image acquisition.

For each run, between 50 and 1000

TRPIV velocity fields were acquired. TSI software, *INSIGHT 3G*[™], was used to process the data. Two sets of raw images (corresponding with Frame A and Frame B) were conditioned independently before vector processing by first scanning each raw image set and creating an image that contained the minimum pixel intensity at every location across the sequence. This minimum intensity image was then subtracted from every image in the sequence, accentuating the particle images and diminishing the effect of constant sources of illumination such as background light, laser glare and noise. The vector fields were determined using a CDIC deformation algorithm described by Wereley and Gui (2001). This four-pass method resulted in an interrogation region of 16 by 16 pixels with 75% overlap, which corresponds to a resolution of slightly more than 2 mm square for the $(141 \text{ mm})^2$ field. The first two passes used a recursive grid to determine integer pixel displacement values. The following two passes employed a four-corner deformation grid to improve measurement accuracy. This processing scheme yielded 97% or higher valid vectors in each field. The algorithm maintains a spatial displacement accuracy of approximately 0.1 pixels, so that the spatial displacement error in the following PIV data is on the order of 2.5% for a particle displacement of 4 pixels ($= U_\infty$). The error associated with temporal variations in the laser pulse synchronization is several orders of magnitude smaller (Adrian 1997).

3 Results

3.1 Force Measurements

Force measurements were taken on the airfoil at a Reynolds number of $Re_c = 2.0 \times 10^5$. The results of the lift coefficient ($C_L = L / \frac{1}{2} \rho U_\infty^2 cb$) vs. angle of attack (α) are presented in Figure 5 for various flap heights (h) in the linear regime of the lift curve. The shape of the lift curve versus angle of attack remains nearly identical for airfoils with Gurney flaps as compared to the control airfoil without a Gurney flap; however, C_L increases by an average of 0.09 for the airfoil with a 1% Gurney flap, by 0.21 for the airfoil with a 2% flap, and by 0.36 for the airfoil with a 4% flap. These trends and the overall curve shapes are consistent with the findings of Wadcock (1987) and Jeffrey et al. (2000).

In addition to the three flapped cases, a “closed” airfoil was also tested. This airfoil shape consisted of the 4% flapped airfoil with the upstream cavity of the airfoil filled in. This case, also recorded in Figure 5, shows an increase in lift coefficient of approximately 0.16, which is slightly less than the 2% flap case; this result seems reasonable since the rear point of the camber line is effectively the same for these two cases, though the camber lines themselves are not the same. By comparing the 4% flap and the closed flap, it is seen that only part of the lift increment can be explained by the mean deflection of streamlines around an asymmetric shape. The remaining increase in lift coefficient must be a direct result of the flow characteristics in the upstream cavity.

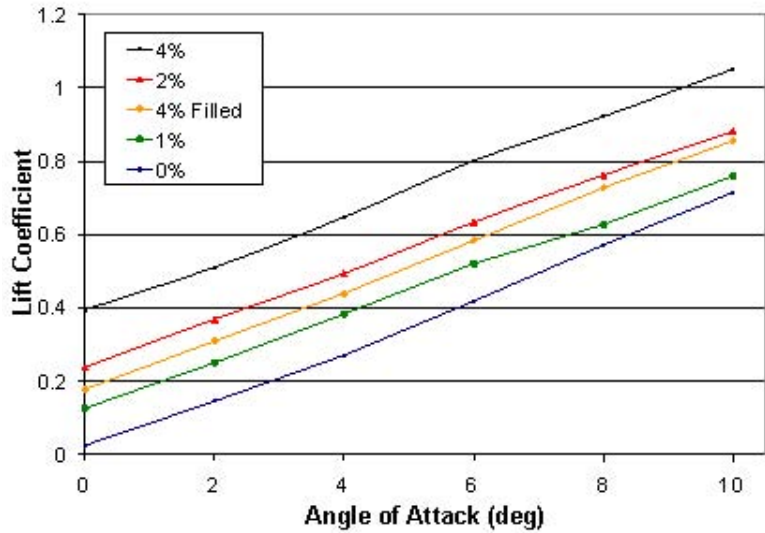


Figure 5: C_L vs. for Gurney flaps of various heights.

3.2 Hot-film Anemometry Measurements

The airfoil without the Gurney flap displayed a frequency spectrum without large dominant peaks. Spectra downstream of the airfoil with the 4% Gurney flap had an obvious dominant peak whose frequency value depended upon the angle of attack. Peak frequencies obtained with both hot-film anemometry and TRPIV are shown in Figure 6 in the form of Strouhal number vs. angle of attack. The Strouhal number is based on flap height (h) and free-stream velocity (U_∞). The plot states that TRPIV frequency analysis matches well with the hot film anemometry and is a valid technique for obtaining the dominant frequency of fluctuating velocity in this case.

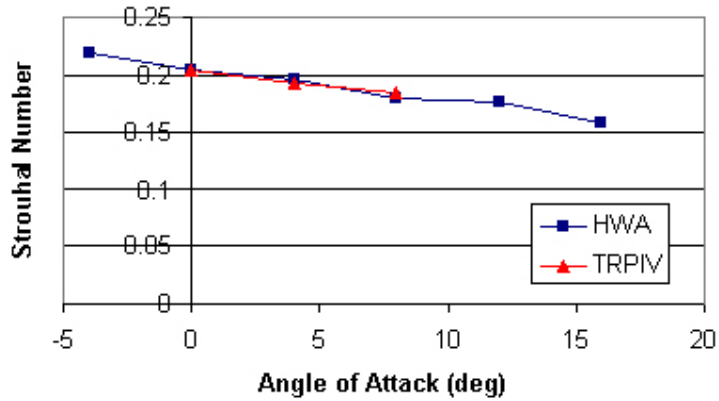


Figure 6: Strouhal number ($St = fh/U$) vs. for 4% Gurney flap.

The frequency analysis suggests the presence of vortices being shed downstream of the Gurney flap. As α increases from -4° to 16° , the Strouhal number decreases approximately linearly from 0.22 to 0.16. Frequency spectra plotted for other airfoil shapes have resulted in similar trends and magnitudes for the Strouhal number (see Jeffrey et al. 2000). This decreasing trend is due to the nature of vortex shedding, where the shedding frequency decreases as the distance between upper and lower shear layers increases. As α increases, the boundary layer thickness on the suction surface increases, thereby increasing this distance, and lowering the shedding frequency (Blake 1986). This trend can also be explained by the idea that the cross-sectional length scale circular to the free stream increases with increasing angle of attack. The absolute shedding frequency must then decrease to maintain a constant Strouhal number based on this scale.

3.3 Ensemble-Averaged PIV Measurements

The time-averaged velocity magnitude field with streamlines can be seen in Figure 7 for a 4% Gurney flap at $\alpha = 0^\circ, 4^\circ, 8^\circ,$ and 12° . Fifty consecutive fields, corresponding with approximately 18 cycles of vortex shedding, were averaged, and the results are normalized by the freestream velocity U_∞ .

The plots show that the area of decreased velocity directly downstream of the Gurney flap increases in length as the angle of attack increases. At $\alpha = 0^\circ$, the zone of strongly reduced velocity (depicted as blue) is compact, and the higher speed flows on either side of the airfoil recover fairly quickly after the separation behind the flap. This recovery takes longer spatially as α is increased. Note also that the wake (or zone of reduced velocity) is turned downward as α increases. The streamlines are also turned downward with increasing α as expected from the lift measurements. The “average” separated region depicted by the streamlines shows a relatively symmetric vortex pair at $\alpha = 0^\circ$ that becomes increasingly asymmetric as α is increased. At $\alpha = 12^\circ$, a negative vortex dominates the area directly downstream of the Gurney, while a more compact, positive vortex has been shifted downstream. These results agree well with the time-averaged velocity fields determined by Jeffrey et al. (2000) and others (see Jang et al. 1998 and Solovitz and Eaton 2004a and b).

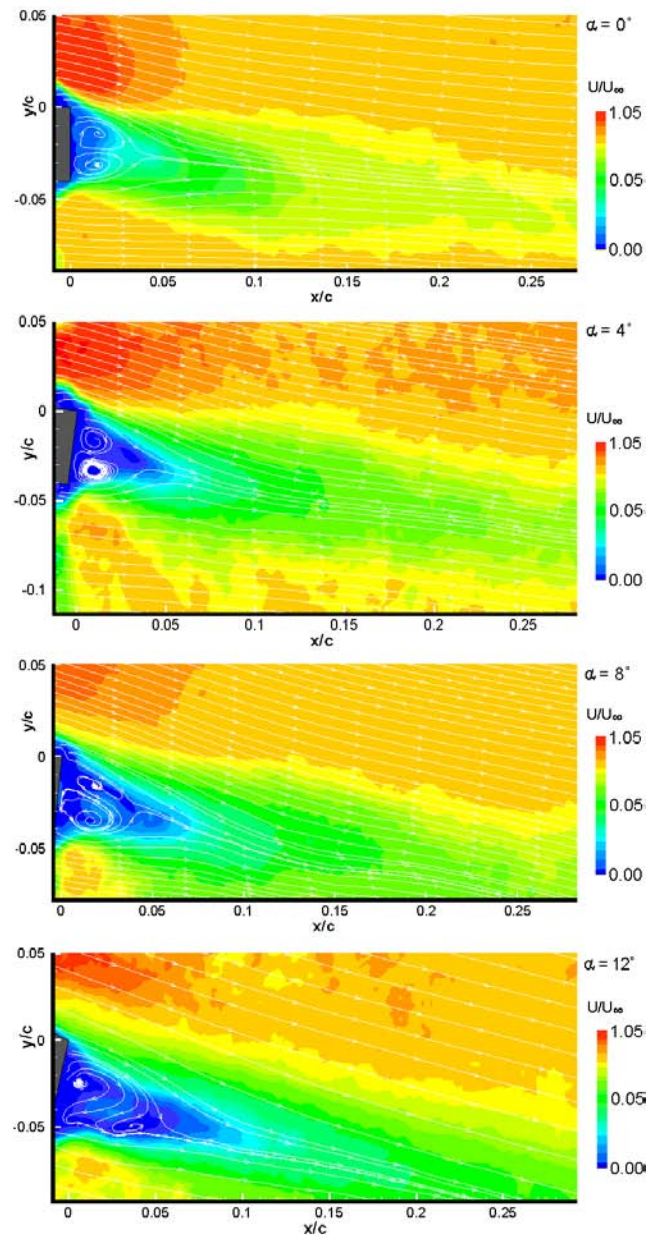


Figure 7: Time-averaged velocity magnitude for 4% Gurney flap with $\alpha = 0^\circ, 4^\circ, 8^\circ$ and 12° , respectively.

3.4 Time-Resolved PIV Measurements

Vortex shedding occurs downstream of trailing edges that support separating shear layers, and the resulting interaction forms the well-known Kármán vortex street. The Gurney flap acts as a bluff body that produces vortex shedding, but its asymmetry yields asymmetries in the wake pattern. Of particular interest in this study was the nature and path of the vortices as they formed and convected downstream.

TRPIV sequences of vorticity and streamwise velocity are shown in Figures 8 and 9 (for $\alpha = 0^\circ$ and $\alpha = 8^\circ$). Each plot is assigned a phase according to the dominant Strouhal number for that angle of attack; specifically, the dominant spectral frequency is divided by the PIV capture rate and shown in terms of percent of one complete shedding sequence. The 0% phase is chosen to coincide with the formation of a vortex, so that the evolution of the vortex can be seen easily in the subsequent plots. The plots reveal

strips of spanwise vorticity (ω) with negative and positive sign that are shed from the upper airfoil surface and Gurney flap tip respectively. In Figure 8 ($\alpha = 0^\circ$), the negative vorticity shed from the upper surface remains focused in the form of a strip that is pulled downward into the flap wake. The positive vorticity shed from the flap tip is spread initially over a larger length scale across the wake and shows greater intermittency in the streamwise direction. Downstream of the trailing edge, the wake develops into an asymmetric Kármán vortex street pattern. The areas of negative vorticity appear more focused than the areas of positive vorticity. The wake also exhibits a net downward flow direction which is expected given the positive lift coefficient for this configuration. The wake asymmetry can be explained partially by the differences in flow direction at the airfoil trailing edge and the flap tip. The presence of the flap generates a local separation upstream so that the streamlines are diverted downward compared with the “no flap” configuration. The measurement of C_L for the closed flap configuration suggests that this is only part of the reason behind the asymmetry.

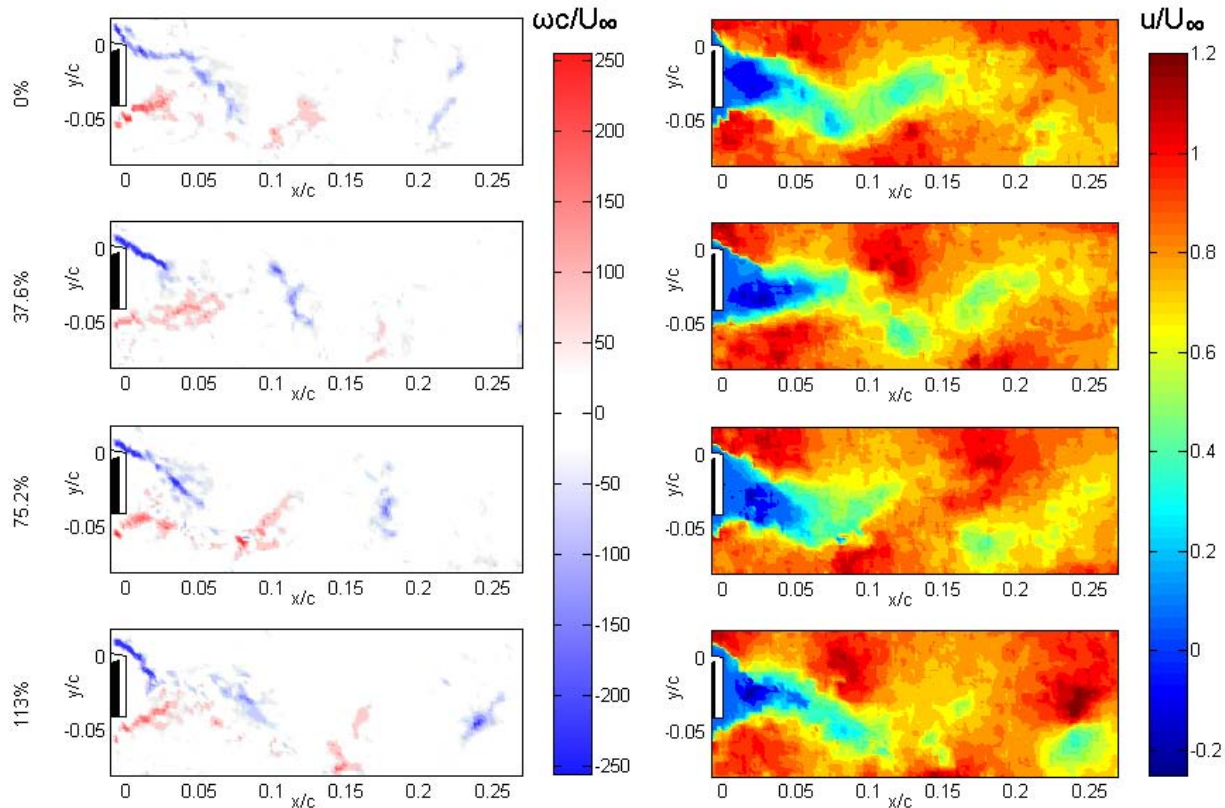


Figure 8: Normalized vorticity ($\omega c/U$) (left), and normalized streamwise velocity (u/U) (right) downstream of the 4% Gurney flap on a NACA 0015 airfoil at $\alpha = 0^\circ$. Phase values on the left indicate the percentage of one complete shedding cycle. The velocity field capture rate was 1000 Hz (2000 fps).

The plots of normalized streamwise velocity (u/U_∞) indicate strong oscillations in magnitude consistent with the presence of a vortex street. In contrast to the time-averaged plot, zones of very low streamwise velocity (shown as cyan) persist downstream to the limit of the field of view. Note the slow moving zone in the bottom right corner of the last plot in the sequence, and also that a very fast moving zone lies immediately above it. This juxtaposition corresponds directly with a compact zone of strong negative vorticity (blue in left sequence) that has traversed across the field. A juxtaposition of opposite sense (cyan lying above dark red) is associated with positive vorticity (red in left plots) that also traverses the field. Though this “vortex” appears to have a similar order of circulation, the magnitude is approximately 14% smaller than the negative vortex bundle. This vortex drops vertically out of the field of view due to the wake asymmetry. One final point is that the velocity magnitude immediately below the flap tip varies significantly indicating intermittent shedding of fluid from the separated zone upstream of the flap.

In Figure 9 ($\alpha = 8^\circ$), the vorticity from the upper surface is again pulled into the flap wake in the form of strips. The ensuing wake is then characterized by increased disorder and asymmetry compared to the $\alpha = 0^\circ$ case. Regions of positive and negative vorticity can be distinguished, but there is less focusing of like structures, which manifest themselves in many smaller patches rather than neat bundles. Also, further downstream of the flap, some small patches of positive and negative vorticity are tightly intertwined suggesting greater disorganization in the wake. The normalized streamwise velocity plots are consistent with the increased disorder seen in the vorticity plots, and the region beneath the flap tip shows increased fluctuations in magnitude compared with the $\alpha = 0^\circ$ case. Note that the low velocity zones (blue and cyan) are broader than for $\alpha = 0^\circ$. As in the time-averaged plot for $\alpha = 8^\circ$, the wake is bent downward beyond the limit of the field depicted.

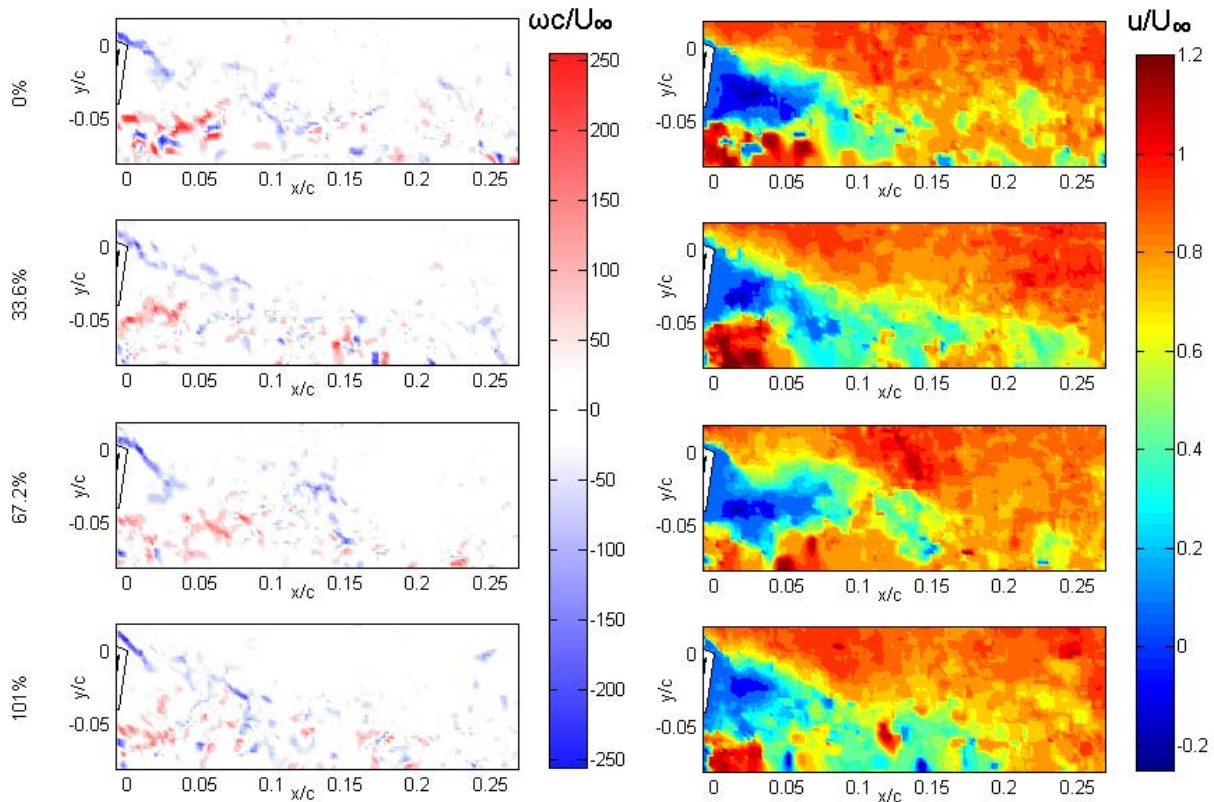


Figure 9: Normalized vorticity ($\omega c/U$) (left), and normalized streamwise velocity (u/U) (right) downstream of the 4% Gurney flap on a NACA 0015 airfoil at $\alpha = 8^\circ$. Phase values on the left indicate the percentage of one complete shedding cycle. The velocity field capture rate was 1000 Hz (2000 fps).

The Gurney flap sequences can be contrasted with a “no flap” sequence shown in Figure 10. As would be expected, this velocity sequence reveals a much narrower wake with much weaker velocity deficits. In addition, any coherent vortical structures are weaker and less defined. When the angle of attack is increased to 8° , the wake remains narrow but is deflected downward as expected.

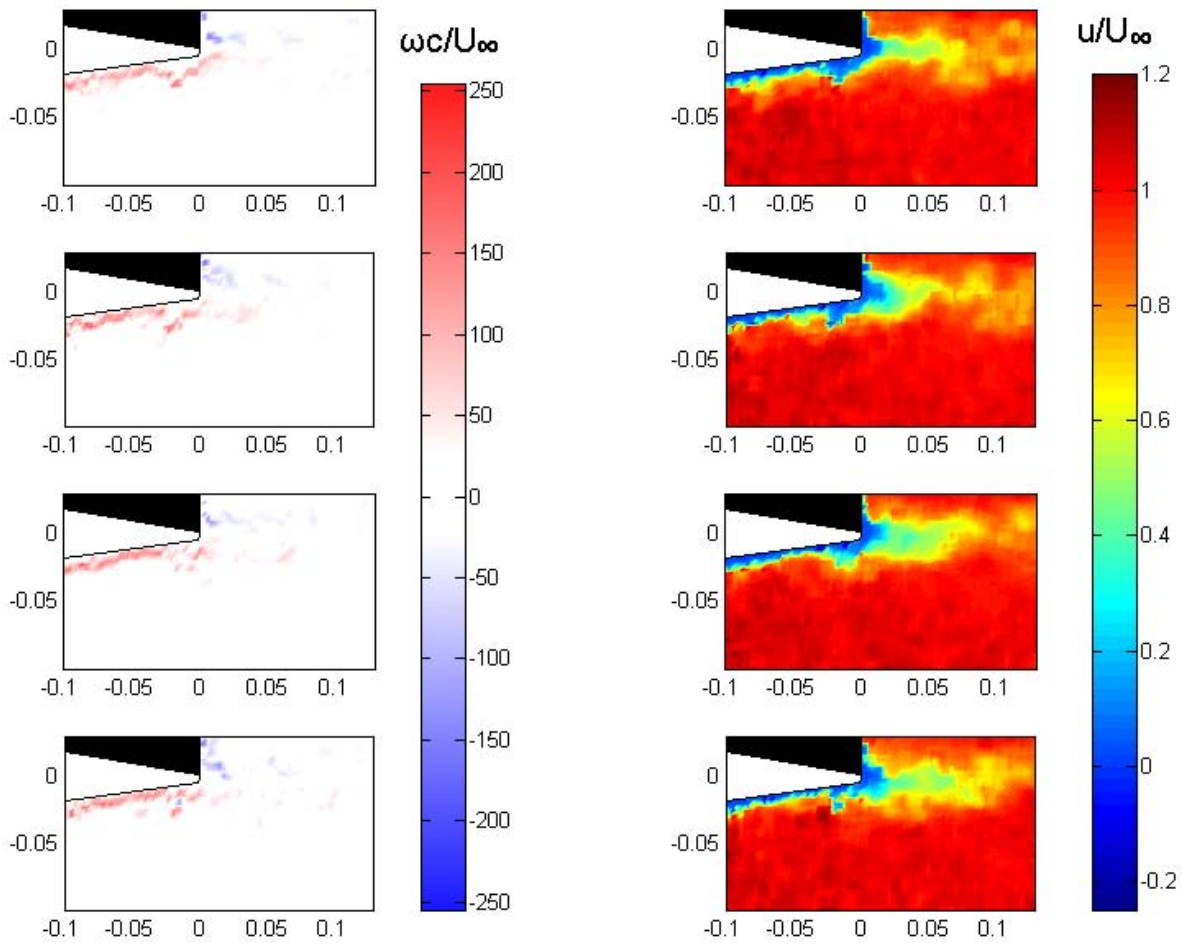


Figure 10: TRPIV sequence captured at 2000 Hz (4000 fps) for the control airfoil with no Gurney flap at $\alpha = 0^\circ$. Column on the left shows normalized vorticity (ω_c/U_∞), while the column on the right shows normalized streamwise velocity (u/U_∞). Phase values are not included as this configuration does not have a dominant shedding frequency.

TRPIV data taken with the laser sheet directed through the top of the wind tunnel allowed the cavity upstream of the Gurney flap to be examined. In this case, the flapped airfoils were inverted compared with those in the previous studies. For ease of comparison with the previous results, the plots in this section have been inverted to match the previous geometries.

Figures 11 and 12 exhibit the 2D swirl strength and the normal velocity (component perpendicular to the streamwise velocity) around the tip of the Gurney flap for $\alpha = 0^\circ$ and $\alpha = 8^\circ$. Two-dimensional swirl is a quantity used to identify vortex cores with significant strength, and orientation normal to the measurement plane. Specifically, it distinguishes fluid swirling about an axis from fluid rotation caused by a shear layer. If the discriminant of the characteristic equation of the two-dimensional velocity gradient tensor is less than zero, then the 2D swirl strength is defined as the imaginary part of its complex root (see Adrian et al. 2000). The swirl is normalized by the freestream velocity and the chord length. Also, the swirl (a positive scalar quantity) is given a sign indicating the direction of the corresponding vorticity. The phase values shown to the left of each plot were calculated based on the Strouhal number determined in the hot film anemometry and TRPIV frequency measurements. The swirl strength plots show distinct alternating positive and negative vortex cores being generated asymmetrically downstream of the flap, with a positive streamwise and negative normal velocity trajectory. Significant swirl zones are not apparent upstream of the flap, most likely because the fluid there does not rotate about a single axis.

For the $\alpha = 0^\circ$ case (Figure 11), the 0% phase plot shows a positive vortex core forming on the downstream edge of the Gurney flap tip. The core then moves downstream and slightly downward in the subsequent phases. Approximately half way through the cycle, a negative vortex core is seen separating from the upper surface, and continuing downstream and slightly downward in the airfoil wake. The normal velocity plot (right column) reveals large upflow and downflow zones associated with the vortices. Note the intermittent downwash immediately upstream of the Gurney flap.

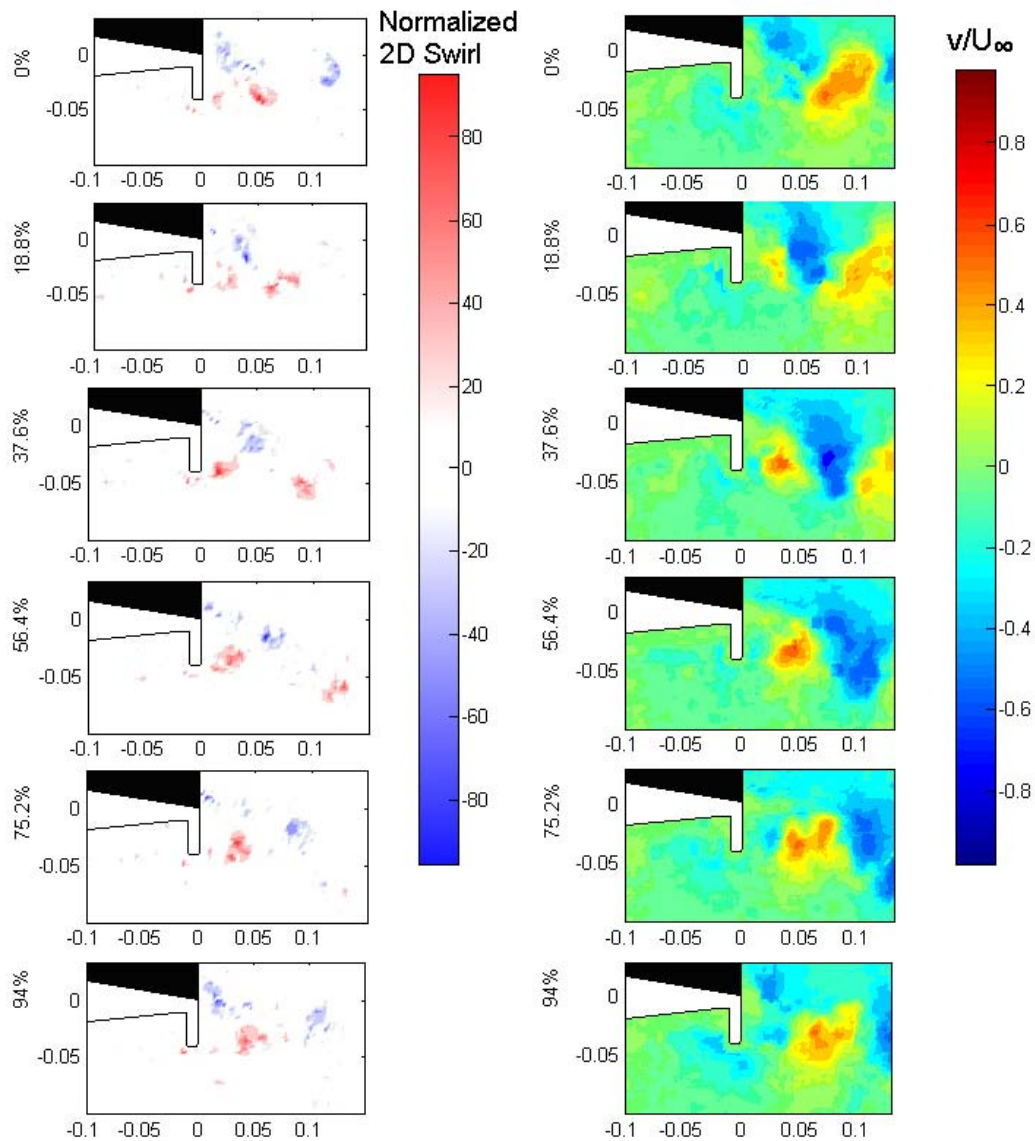


Figure 11: One full primary vortex shedding sequence for the case of a 4% Gurney flap at $\alpha = 0^\circ$ captured at 4000 Hz (8000 fps), every other frame is shown. The phase values to the left of each plot represent the percentage of one complete vortex shedding sequence. The plots display the normalized 2D swirl strength (left) and the normalized normal velocity (v/U_∞) (right).

Figure 12 plots the $\alpha = 8^\circ$ case. The same general structure can be seen in terms of the vortex shedding; however, consistent with the previous vorticity plots (Figure 8), the ensuing wake is less organized, as can be seen by the red counterclockwise cores that are distributed over a larger spatial area for $\alpha = 8^\circ$. Also, the shapes of the upwash and downwash zones appear similar, but the local velocity magnitudes are somewhat weaker.

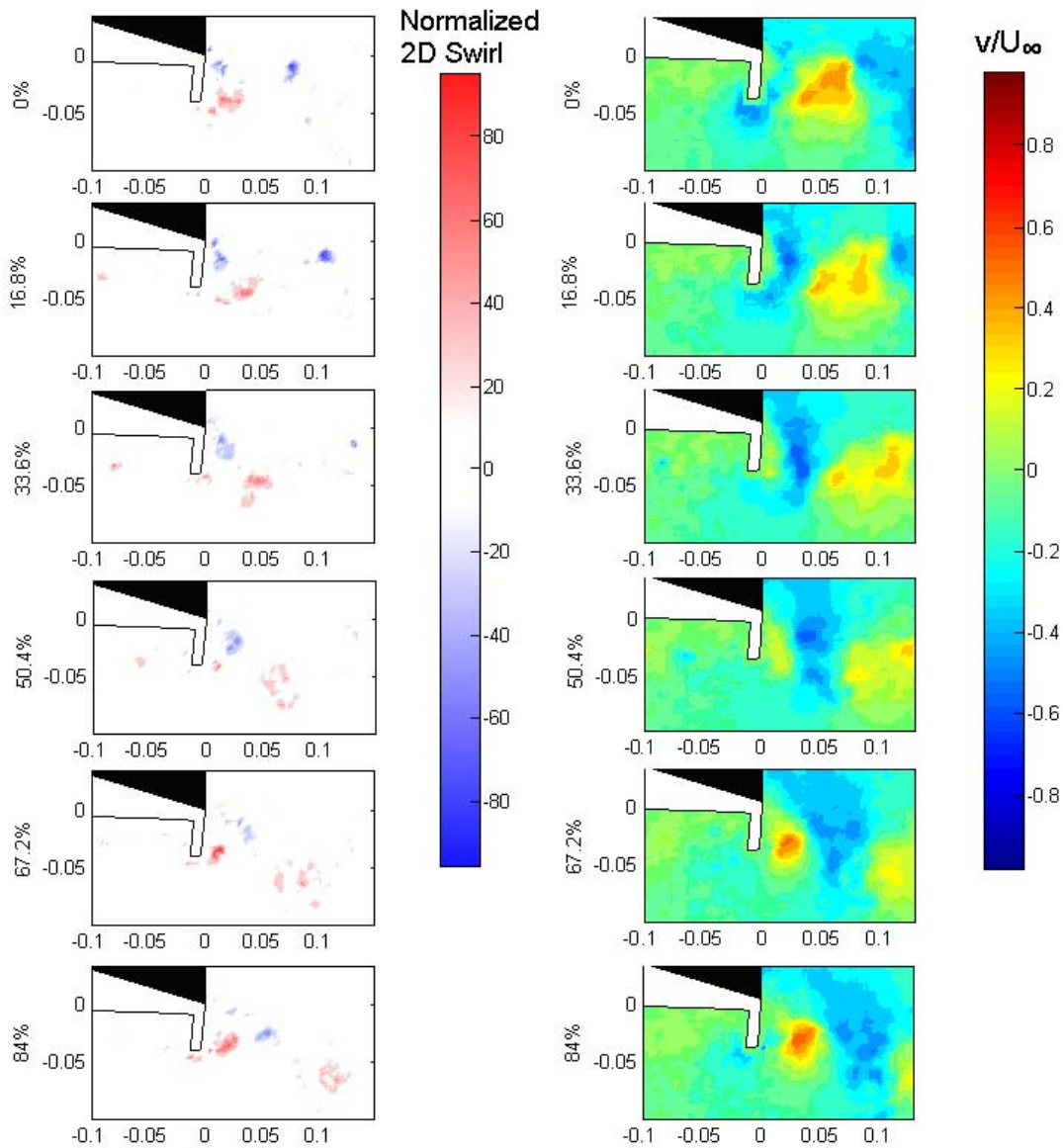


Figure 12: One full primary vortex shedding sequence for the case of a 4% Gurney flap at $\alpha = 8^\circ$ captured at 4000 Hz (8000 fps), every other frame is shown. The phase values to the left of each plot represent the percentage of one complete vortex shedding sequence. The plots display the normalized 2D swirl strength (left) and the normalized normal velocity (v/U_∞) (right).

Careful studies of the time-resolved movies of streamwise and normal velocity show that the asymmetry of the vortex street is due at least partially to the presence of two shedding modes off of the flap tip. A representative sequence for $\alpha = 0^\circ$ is shown in Figure 13. In the cavity upstream of the flap tip, fluid recirculates. Periodically, some of this fluid is ejected below the flap tip (see the vectors in the last two phases shown). This process generates a local surge in streamwise velocity with some downward orientation.

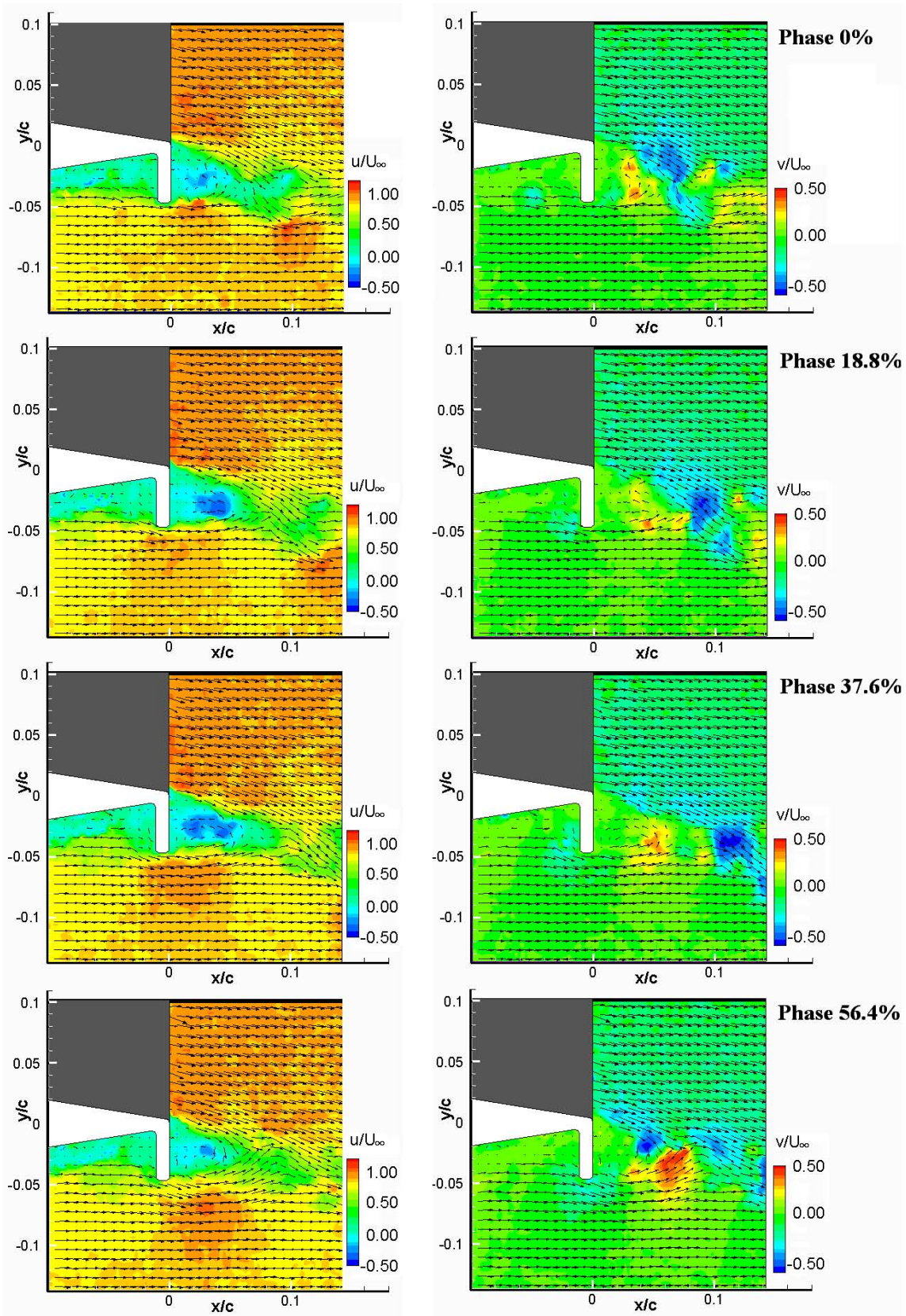


Figure 13: Consecutive instantaneous velocity fields of the airfoil with 4% Gurney flap and $\alpha = 0^\circ$ acquired at 2000 Hz (4000 fps) corresponding to phase positions of 0%, 18.8%, 37.6, and 56.4%. Instantaneous velocity vectors are overlaid on normalized streamwise velocity (u/U) (left) and normalized normal velocity (v/U) (right).

Figure 14 displays a schematic of the two modes of vortex shedding seen in the data and in the previous figure. PIV sequences and wake visualization show that the flap acts as a forward facing step which traps fluid in the form of a weak and generally disorganized positive vortex (shown in green). The fluid cannot escape above through the airfoil, or downstream due to the flap. Neither can the slow moving fluid escape downward as this would require it to cross the fast-moving, nearly streamwise velocity present below the airfoil but outside of the boundary layer. While slow-moving boundary layer fluid from beneath the airfoil is accumulating in the cavity upstream of the Gurney flap, the airfoil and flap support a shape resembling an asymmetric solid body with a blunt trailing edge. Streamlines nominally conform to this shape before shedding off of the trailing edge with a frequency of 376 Hz ($St = 0.20$) for the case of $\alpha = 0^\circ$. After some amount of time, the fluid that has been accumulating in the upstream cavity has grown spatially, both downward toward the flap tip and also upstream in the direction of the leading edge, to the point where its normal length scale is near that of the Gurney flap height. When this occurs, the trapped vortex achieves enough energy to penetrate or push downward the layer of high streamwise velocity just below the Gurney flap. This is manifested in a burst of velocity downward, as the recirculating fluid escapes the cavity, and an accompanying burst in streamwise velocity. This downward velocity component induces a similar downward component of velocity on the fluid and vortex structures directly downstream of the Gurney flap. During this instant, the flow downstream of the flap attains a relatively large component of negative normal velocity that momentarily increases the circulation on the airfoil, thus increasing the lift. This also helps to explain the shape and deflection of the time-averaged velocity magnitude plots in Figure 7. A histogram of the normal velocity measured at the tip of the Gurney flap can be seen in Figure 15; its bimodal distribution indicates normal velocity in primarily two modes, when the upstream vortex is weak but gaining strength, and when the vortex is expunged from the cavity. The data for the 2% Gurney flap shows a similar bimodal normal velocity distribution.

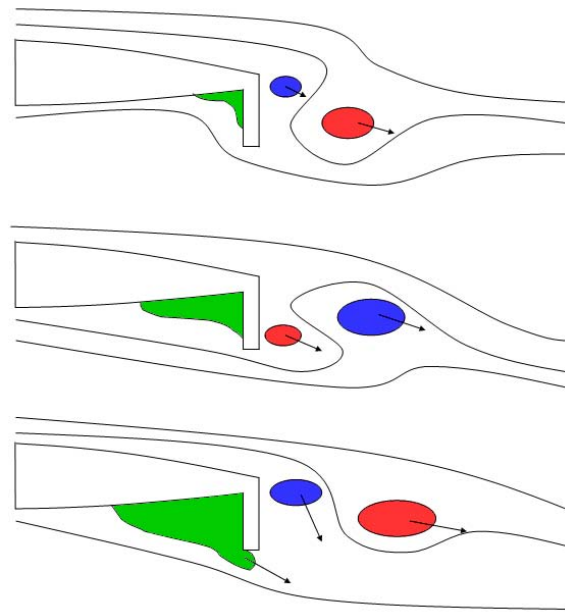


Figure 14: Schematic of the bimodal vortex shedding occurring at the trailing edge of the airfoil with a Gurney flap. Positive vorticity is indicated in red; negative vorticity is indicated in blue. The green areas represent fluid “trapped” in the upstream cavity. Arrows represent general trajectories of flow structures.

Observations of TRPIV movies and spectral analysis upstream of the Gurney flap using hot-film anemometry both indicate that the frequency at which the trapped fluid is expunged from the upstream cavity is somewhat lower than that of the Kármán shedding frequency.

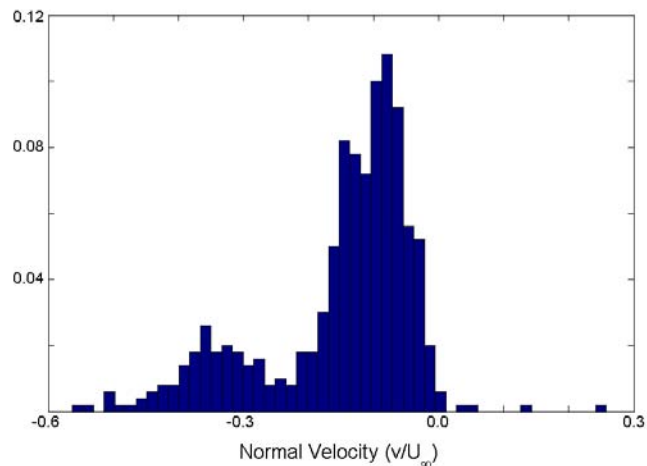


Figure 15: Normalized normal velocity PDF at the point below the 4% Gurney flap tip at $\alpha = 0^\circ$.

Representative spectra from both hot-film anemometry and TRPIV are shown in Figure 16 for the case of the 4% Gurney flap. The difference in energy magnitude between the two methods is due to the process by which the spectra were calculated. The hot-film data used the total velocity measured, while the TRPIV data used only the fluctuating component of the normal velocity. At $\alpha = 0^\circ$, both methods display an obvious peak at the downstream Kármán shedding frequency. For the $\alpha = 8^\circ$ case, the single dominant peak is shifted to a slightly lower frequency due to the increased normal length scale discussed earlier. A second, weaker and broader peak emerges at an even lower frequency representing the fluid shedding from the upstream cavity. (The existence of this weaker peak was not mentioned by Jeffrey et al., 2000). The combination of the two HWA plots suggests that at low angles of attack, the recirculation zone upstream of the flap is shedding fluid in a manner that does not exhibit a strongly periodic event. At higher angles of attack, however, the upstream cavity forms a niche that more easily blocks fluid from passing into the downstream wake. For this reason, a more structured event is required to expunge the build-up of slower-moving fluid. This is manifested in a more periodic form of upstream shedding.

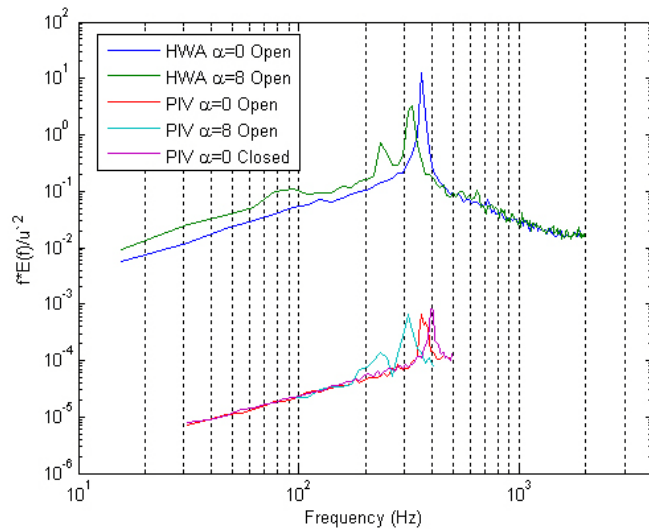


Figure 16: Frequency spectra captured with hot-film anemometry and time-resolved PIV plotted for the 4% Gurney flap. The blue and green lines indicate hot-film data for the case of $\alpha = 0^\circ$ and 8° , respectively. The red and teal lines indicate TRPIV data for the cases of $\alpha = 0^\circ$ and 8° . The magenta line indicates TRPIV data for the case of $\alpha = 0^\circ$ in the closed flap configuration.

The TRPIV spectral plot for the case of the 4% closed flap is also plotted (magenta). Notice the distinct shift in the single dominant peak to a higher shedding frequency, as well as the increase in energy. The closed flap configuration has a much more focused form of downstream vortex shedding since the pattern is not occasionally interrupted by fluid suddenly shed from upstream. The frequency increase is likely due to the fact that the time-averaged cross-sectional length scale perpendicular to the free stream is smaller for the closed-flap case because it does not experience the occasional increase in boundary layer thickness on the flap side of the airfoil due to the upstream shedding. Observations of the time-resolved PIV velocity fields confirm that the secondary shedding mode exists only in open flap configurations.

Figure 17 displays the locations where hot-film spectral measurements were taken for the case of the airfoil at $\alpha = 8^\circ$ with the 4% Gurney flap. Also shown are the resulting Strouhal numbers based on the freestream velocity (U_∞), Gurney flap height (h), and the frequency peaks seen in the spectra. The dominant frequency in the upstream region of the cavity corresponded with $St = 0.13$. Downstream of the cavity, this peak was also apparent in addition to the stronger peak corresponding with the Kármán shedding frequency, $St = 0.18$. This pattern of peak frequencies further suggests that there exists in the cavity upstream of the flap a mode of fluid shedding which is distinct from the Kármán shedding that dominates the downstream wake. In addition,

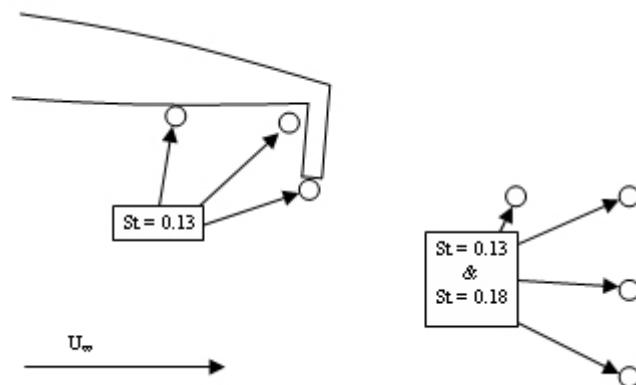


Figure 17: Peak Strouhal numbers ($St = fh/U_\infty$) observed from hot-film spectra at various locations.

the upstream and downstream shedding are coupled, in that both types affect the vortex formation and interaction downstream. The TRPIV visualization shows that the upstream activity has a significant effect on the downstream wake of the airfoil; namely, contributing a net downward velocity to the wake. The coupled shedding behavior described here was also observed at $\alpha = 0^\circ$ though in a much less periodic manner. Hot-film measurements for the airfoil with no Gurney flap revealed no equivalent spectral peaks. Further, the peak at $St = 0.13$ was not observed at locations further than one-third chord length upstream of the 4% flap.

4 Conclusions

The velocity field sequences generated by the TRPIV method revealed a mode of vortex shedding not previously observed or postulated in experimental or numerical investigations of flow around Gurney flaps. A loosely organized vortex forms and grows in the cavity upstream of the flap until it is expunged into the airfoil wake where it interacts with the Kármán vortex street that forms directly downstream of the flap. This upstream vortex shedding was not present in a case with a “filled-in” flap that generated approximately half the lift increment of the open-cavity case. Thus, it appears that a significant part of the lift increment produced by the Gurney flap results directly from the upstream shedding and its influence on the trailing wake.

While it is somewhat intuitive that the Gurney flap increases lift by adding to the effective camber of the wing, the less-obvious advantage of the Gurney flap lies in the complex flow structure surrounding it. TRPIV is an effective tool in studying this structure due to the presence of recirculation, unsteadiness, and coherent vortices that form at more than one frequency. TRPIV provides a field-based temporal history that can capture the dynamics of the flow. The Gurney design, which includes both a blunt trailing edge and a single-sided leading edge, generates both a “standard” wake of alternating counter-rotating vortices with fairly predictable frequency and the additional single-signed vortices shed from the cavity upstream of the flap tip at a lower frequency. The flow sequences reveal that the intermittent release of fluid from the cavity induces a net negative normal velocity on the airfoil wake increasing the circulation, and thus the lift. This phenomenon served to increase the lift at every angle of attack measured.

Although the lift increment for a given flap length is fairly constant for different angles of attack, examination of TRPIV sequences and spectra suggests that the coherence of the shedding of upstream fluid increases and the related shedding frequency decreases with increasing angle of attack. Also, since the volume of “trapped” fluid is expected to decrease with decreasing flap length, it is expected that the corresponding shedding frequency would increase. This hypothesis as well as the details of the specific relationship between the two shedding modes under different parametric conditions will be examined in future work. Further, it would be interesting to see if the dual-mode shedding observed could be captured by computational methods suited for modeling unsteady separated flows.

5 Acknowledgements

The authors thank the University of Minnesota Aerospace Engineering and Mechanics Department for the use of the facilities and for fabrication of the airfoil test sections.

6 References

- Adrian R (1991), “Particle-Imaging Techniques for Experimental Fluid Mechanics.” University of Illinois, *Annual Review Fluid Mechanics*, Vol. 23, pp 261-304.
- Adrian R (1997), “Dynamic Ranges of Velocity and Spatial Resolution of Particle Image Velocimetry.” *Meas. Sci. Technol.* 8, pp. 1393–1398.
- Adrian R; Christensen K; Liu Z; (2000), “Analysis and interpretation of instantaneous turbulent velocity fields.” *Exp. Fluids* 29, pp. 275-290.

- Blake W (1986), "Mechanics of Flow-Induced Sound and Vibration" Vol. II, *Academic Press, Inc.*, pp. 756-782.
- Jacobs E; Anderson R (1930), "Large-Scale Aerodynamic Characteristics of Airfoils as Tested in the Variable Density Wind Tunnel," *NACA Langley Memorial Aeronautical Laboratory (Langley Field, VA, United States) NACA TR 352*, pp. 421-50.
- Jacobs E; Sherman A (1937), "Airfoil section characteristics as affected by variations of the Reynolds number," *NACA Langley Memorial Aeronautical Laboratory (Langley Field, VA, United States) NACA Report 586*, pp. 41.
- Jang C; Ross J; Cummings R (1998), "Numerical investigation of an airfoil with a Gurney flap." *Aircraft Design 1*, pp. 75-88.
- Jeffrey D; Zhang X; Hurst D (2000), "Aerodynamics of Gurney Flaps on a Single-Element High-Lift Wing," *Journal of Aircraft*, Vol. 37. No. 2, pp. 295-301.
- Liebeck R (1978), "Design of subsonic airfoils for high lift." *Journal of Aircraft 15*(9), pp. 547-61.
- Maughmer M; Lesieutre G; Koopmann G (2003), "Miniature Trailing Edge Effectors for Rotorcraft Applications." *Natl. Rotorcraft Tech. Center*.
- Neuhart D; Pendergraft O (1988), "A water tunnel study of Gurney flaps." NASA TM 4071.
- Solovitz S; Eaton J (2004), "Spanwise Response Variation for Partial-Span Gurney-Type Flaps," *AIAA Journal*, Vol. 42, No. 8, pp. 1640-1643.
- Solovitz S; Eaton J (2004), "Dynamic Flow Response Due to Motion of Partial-Span Gurney-Type Flaps," *AIAA Journal*, Vol. 42, No. 9, pp. 1729-1736.
- Storms B; Jang C (1994), "Lift Enhancement of an Airfoil Using a Gurney Flap and Vortex Generators," *J. Aircraft*, Vol. 31, No. 3, pp. 542-547.
- Wadcock A (1987), "Investigations of low-speed turbulent separated flow around airfoils." NASA CR 177450.
- Wereley S; Gui L (2001), "PIV measurement in a four-roll-mill flow with a central difference image correction (CDIC) method," *4th International Symposium on Particle Image Velocimetry*, Göttingen, Germany, September 17.
- Wynbrandt J (2002), "Ban, or Banner?" *AOPA Pilot*, pp. 97-101.

This paper was originally published in "Experiments in Fluids," Volume 41, Number 2/August 2006, publisher Springer Berlin/Heidelberg. The original publication is available at www.springerlink.com.

TSI Incorporated – 500 Cardigan Road, Shoreview, MN 55126 U.S.A

USA	Tel: +1 800 874 2811	E-mail: fluid@tsi.com	Website: www.tsi.com
UK	Tel: +44 149 4 459200	E-mail: tsiuk@tsi.com	Website: www.tsiinc.co.uk
France	Tel: +33 491 11 87 64	E-mail: tsifrance@tsi.com	Website: www.tsiinc.fr
Germany	Tel: +49 241 523030	E-mail: tsigmbh@tsi.com	Website: www.tsiinc.de
India	Tel: +91 80 41132470	E-mail: tsi-india@tsi.com	
China	Tel: +86 10 8260 1595	E-mail: sibeijing@tsi.com	
Singapore	Tel: +65 6595 6388	E-mail: tsi-singapore@tsi.com	



Contact your local TSI Distributor or visit our website www.tsi.com for more detailed specifications.